Plasma potential control in a magnetized plasma column using a thermionic cathode

F Pagaud, V Dolique, S Vincent, B Trotabas, R Gueroult, N Plihon

Plasma potential control in a magnetized plasma column using a thermionic cathode

F Pagaud[1], V Dolique[1], S P H Vincent[1,2], B Trotabas[3], R Gueroult[3] and N Plihon[1]

[1] Univ Lyon, ENS de Lyon, CNRS, Laboratoire de Physique, F-69342 Lyon, France
[2] École Polytechnique Fédérale de Lausanne (EPFL), Swiss Plasma Center (SPC), CH-1015 Lausanne, Switzerland
[3] LAPLACE, Université de Toulouse, CNRS, INPT, UPS, 31062 Toulouse, France

Abstract. The ability to drive the plasma potential in a magnetized plasma column using strongly negatively biased emissive cathode is experimentally demonstrated. By analyzing an extensive experimental dataset, and in particular the evolution of the radial profiles of the plasma parameters (plasma density, electron temperature, plasma potential) obtained for various background magnetic field and neutral filling pressure, we first show that current injection from a negatively biased cathode offers an additional level of control as compared to a cold cathode. The radial potential drop across the plasma column, *i.e.* perpendicular to the magnetic field, is observed to be proportional to the current injected at the cathode. The experimental observations are in excellent qualitative agreement with recent theoretical predictions [*Plasma Sources Sci. Technol.* **31** 025001 [1]], in particular for the scaling B^2/n_n of the plasma potential drop with magnetic field B and neutral filling pressure n_n. However, the experimental dataset also reveals the existence of a strong electron sheath (up to a few times the electron temperature) at the outer edge of the plasma column, which is not currently included in the modelling.

Keywords: biasing, conductivity, perpendicular electric field, thermionic emission, electric potential control, electron sheath

Submitted to: *Plasma Sources Sci. Technol.*

1. Introduction

The local electric field in magnetized plasmas has a major impact on the global plasma dynamics and stability. This leads to an inhomogeneous $\mathbf{E} \times \mathbf{B}$ drift velocity $v_{\mathbf{E}\times\mathbf{B}}$ and strong local shears, which can trigger low-frequency instabilities. In the context of fusion, a strong correlation was observed between the presence of a sharp increase in plasma potential at the plasma edge, *i.e.* a transport barrier, and a sudden rise in plasma density, illustrating the essential role of the plasma potential profile in L-H transitions [2, 3]. Further experiments highlighted the influence of the transport barrier on the prevention of large-scale turbulent eddies, thus inhibiting turbulence and reducing particle transport to the wall [4, 5]. Controlling the local electric field in magnetized plasmas is therefore of major interest. Adjusting the $v_{\mathbf{E}\times\mathbf{B}}$ rotation profile of a magnetized plasma, through control of the plasma potential ϕ_p, could also find practical applications such as advanced mass separation technologies [6, 7], as envisioned for nuclear spent fuel reprocessing and rare earth recycling [8, 9].

An attractive solution to achieve such control is to use biased electrodes. In low-temperature plasma devices, biasing has been shown to have a direct impact on the plasma potential profile [10]. It affects the global plasma stability [11, 12] by either triggering flute modes [13], drift waves [13, 14] and Kelvin-Helmholtz instabilities [15], or suppressing instabilities [11, 12, 16]. In general, plasma potential tailoring allows flow control [6] and improved plasma confinement [17, 18]. Hence, electrodes appear as a new control parameter to explore the effect of plasma rotation on low-frequency instabilities [19, 20] and turbulence [21]. This method can also be extended to higher electron temperatures and density in a tokamak configuration [22]. In most of these studies, cold biased electrodes were used. Although cold ring electrodes have proven effective to control the radial potential profile under certain conditions [10, 13, 23], results were inconclusive under a number of other conditions [24].

To understand these limitations, simple theoretical models were recently proposed to describe the impact of a positively biased electrode [25] or a negatively-biased cold electrode [26–28] (*i.e.* a cathode) on the plasma potential. These models compute the plasma potential required for an equilibrium current to be sustained from the cathode to the grounded walls, given the conductivity (or resistivity) in the discharge volume. In a magnetized plasma, a key element controlling the plasma potential is hence the ratio of parallel to perpendicular conductivity $\sigma_\parallel/\sigma_\perp$ [24, 26, 29]. With a cold electrode, the current density at the cathode cannot exceed the ion saturation current. Therefore, when the ion current at the cathode is sufficiently large, the plasma potential is controlled by the value of the ion saturation at the cathode and by the perpendicular resistivity ($1/\sigma_\perp$). This sets upper bounds on the control of the plasma potential. On the other hand, using an emissive cathode allows an increased current injection through the plasma, and thus an extended control on the plasma potential.

In support of this analysis, there have been recent experimental observations of enhanced effects from emissive cathodes, both on plasma properties [30] and on flow control [31, 32]. Emissive cathodes were also shown to have a strong impact on waves and instabilities, as both the plasma potential profile and the plasma density gradients are modified under strong current injection. For instance, intensification of electron-ion hybrid instability [33], spoke generation [34], drift-Alfvén modes induced turbulence [35] or even Kelvin-Helmholtz suppression [34] have all been reported in strongly-emissive regimes. For the purpose of flow control, an important question then is whether emissive cathodes can indeed improve control over the plasma potential.

The present article aims at addressing this question by comparatively investigating the effect of non-emissive and strongly-emissive cathodes in a high-density radio-frequency generated weakly magnetized plasma column. Comparison with models is used to interpret data, but also to point to models' shortcomings that will need to be addressed to allow for quantitative modeling of the effect of emissive cathodes. First, the experimental apparatus is introduced in section 2. Using this setup, the effect of electron injection on plasma properties for a set of different experimental conditions is demonstrated in section 3, underlining in particular how current injection enhances control over the plasma potential. These experimental results are then compared with predictions from the model derived by Trotabas and Gueroult [1], recalled in section 4. The results are compared in section 5 and it is found that the proposed model provides robust physical arguments to interpret and forecast qualitatively the behavior of the obtained results, though the model underestimates the measured potential variations by a factor of about five. Conclusions are drawn in section 6.

2. Experimental setup

The experimental results reported in this article were obtained in the Von-Kármán Plasma (VKP) experiment [36], depicted in figure 1a). The stainless steel cylindrical chamber is 20 cm in diameter and 80 cm long. We use a Cartesian coordinate system, and choose the z-axis along the axis of the vacuum

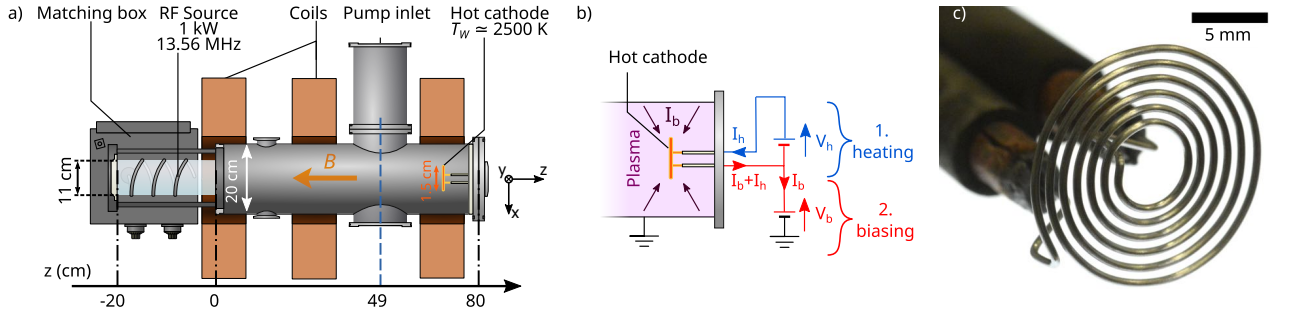

Figure 1: *a)* Sketch of the experimental setup. *b)* Electrical circuit used for heating and biasing the cathode. *c)* Photograph of the spiral tungsten filament used for the thermionic cathode.

chamber. Argon is injected at $z = 16$ cm, near the source tube, at a regulated pressure p_0 of 1 or 2 mTorr. The turbo-molecular pump is located at $z = 49$ cm. The plasma is generated by a 1 kW, 13.56 MHz radio-frequency inductive source wound around an 11 cm wide borosilicate tube. This smaller tube is connected in the plane $z = 0$ cm to the main vacuum chamber. The antenna is fed by a power supply, and the output impedance is matched using a manual L-type matching box such that the reflected power is less than 20 W. The axial confining magnetic field is generated by three Bitter coils placed along the stainless steel cylinder. The amplitude of the field B varies along z, with an average ranging from 170 to 340 G.

An emissive cathode made of a tungsten filament wound in a spiral shape, shown in figure 1c), is placed at the center of the plasma column at the opposite end relative to the source ($z = 72$ cm). The cathode is a $r_W = 0.253$ mm radius tungsten wire rolled up on itself over 6.25 turns to form an Archimedean spiral of external radius $r_b = 0.76$ cm and total length $l_W = 198$ mm for a total filament surface $\mathcal{A} = 2\pi r_W l_W = 314$ mm^2. An overview of the cathode operation is provided here, while the details are described elsewhere [37]. The electrical boundary conditions of the cylinder end plates are chosen insulating: an alumina ring (110 mm inner diameter, 197 mm outer diameter) is installed at $z = 0$ cm and a boron nitride disk (195 mm outer diameter) is installed at $z = 80$ cm. The borosilicate source tube ends in a 110-mm diameter boron nitride disk.

Spatial profiles of the plasma density n, the electron temperature T_e and the plasma potential ϕ_p are respectively performed using an advanced 3-tips probe [19, 38] and an emissive probe, made from a thin 0.15-mm diameter thoriated tungsten filament heated by a constant current up to nearly 5 A, and analyzed using the floating point technique [39]. Note that the 3-tips probe requires a single-Maxwellian electron energy distribution function, which has been confirmed by Langmuir probe measurements (see Supp. Mat. A). The probes were inserted radially at $z = 49$ cm, *i.e.* ~ 25 cm away from the cathode, along the x-axis. To keep the whole apparatus in a steady thermal state, the operation of the plasma is pulsed: the plasma is sustained over typically 5 seconds with a repetition period of 30 s. Since the thermal equilibrium timescale of the hot cathode is of a few seconds, data are acquired only when a stable operation regime is reached during the last two seconds of the biased phase (See Supp. Mat. B). The experiment is fully automated to allow high repeatability and reproducibility of the plasma. The level of shot to shot reproducibility, estimated from a series of 40 shots at the plasma column center, was $\pm 0.6\%$ for the ion saturation current of a Langmuir probe, with a standard deviation of 0.2%. Spatially-resolved scans of the plasma parameters were performed sequentially: the parameters at a given location were acquired during one shot, and the probe was then translated before the next shot.

Measurements were achieved by retracting the probe from $x = -2$ cm to $x = 10$ cm through a DN 160 access port on a lateral recess extending beyond $x = 10$ cm (see figure 1). Note that errorbars displayed for n and T_e result from uncertainties in probe dimensions, while errorbars for ϕ_p correspond to the standard deviation of the signal (*i.e.* correspond to temporal fluctuations). Typical plasma parameters range from 1 to 4×10^{18} m^{-3} for the plasma density and from 3 to 4.5 eV for the electron temperature in the absence of a cathode [19]. The present study focuses on three configurations in which the neutral pressure and the magnetic field were varied as indicated in table 1. The corresponding $\omega_{c,i}/\nu_{in}$ ratios are indicated in table 1, with $\omega_{c,i} = eB/m_i$ the ion cyclotron frequency and ν_{in} the ion-neutral collision frequency (e being the elementary charge, and m_i the ion mass). The expression for ν_{in} is detailled in Supp. Mat. G and is computed using n_n according to the neutral gas filling pressure at the neutral temperature $T_n = 400$ K, and ion temperature $T_i = 0.2$ eV (respectively 0.28 and 0.45 eV) for configuration I (resp. II and III) [40]. The

radio frequency power was kept constant at 1 kW in all three configurations.

Table 1: Control parameters for the three investigated configurations.

Configuration	I	II	III
Magnetic field B (G)	170	240	340
Ar pressure (mTorr)	1	2	1
$\omega_{c,i}/\nu_{in}$	1.2	0.7	1.6
B^2/n_n (vs config. I)	1	1	4
V_b/T_e	10 & 15	13 & 20	13 & 20
$\Xi = I_{em}/I_{is}$	[1;25]	[1;25]	[1;25]
$\chi = T_e/(R_\perp I_{is})$	750	650	160

The goal of this article is to investigate the ability to control the plasma potential profile using a thermionic emissive cathode placed at the center of the plasma column. As shown in figure 1b), the filament is Joule-heated using a heating DC power supply that sets the heating current I_h, leading to averaged temperatures of up to 2800 K. During a plasma shot, the cathode is then negatively biased to the potential V_b with respect to the ground using a DC biasing power supply. Note that the value of V_b is algebraic. In the current work, V_b is negative, resulting in strong thermionic emission. The total current I_b flowing from the plasma to the cathode is hardware-limited to 15 A. The legs of the filament are mechanically locked in 4 mm diameter copper rods (insulated from the plasma by alumina tubes) which feed the current to the cathode. The total current at the cathode reads

$$I_b = I_{em} + I_{is} - I_e \tag{1}$$

with I_{em} the thermionic emission from the cathode, I_{is} the ion saturation current and I_e the electron current from the plasma. All currents are positive-definite. Both I_{em} and I_e are electron currents; however, they flow in opposite directions and therefore contribute in opposite ways to the current flowing at the cathode. Besides, note that cathode biasing is always strong before plasma potential, so that the ion current is considered as saturated. Since the incident energy of ions at the cathode remains limited ($\leq$ 50 eV) and the secondary emission rate of argon on tungsten is relatively low [41], contributions from secondary electron emission to the current balance are neglected [42]. Thermionic emission is governed by the cathode temperature T_W according to Richardson law [43]. Then, the above-mentioned currents can be written as

$$I_{em} = A_{\mathrm{g}} \mathcal{A} T_W^2 \exp\left(-\frac{eW}{k_{\mathrm{B}} T_W}\right) \tag{2}$$

$$I_{is} = \mathcal{A} n e \sqrt{\frac{eT_e}{m_i}} \tag{3}$$

$$I_e = I_{is} \exp\left(\Lambda + \frac{V_b - \phi_p}{T_e}\right) \tag{4}$$

with $A_{\mathrm{g}} = 6\times10^5$ A(K^{2}m^2)$^{-1}$ the Richardson constant for tungsten, W = 4.54 eV the work function of tungsten, k_{B} the Boltzmann constant, and $\Lambda = \ln\left(\sqrt{2m_i/(\pi m_e)}\right)$ a sheath parameter with m_e the electron mass. The Schottky effect was shown to be negligible in the present experimental conditions [37].

Because of the strong dependence of the thermionic current on the cathode temperature, a precise determination of T_W is crucial to compare data with models. Here thermionic emission is first estimated using an averaged temperature $\overline{T_W}$ from the measurement of the cathode resistance $V_h/I_h = \rho_W l_W/(\pi r_W^2)$, with ρ_W the electrical resistivity of tungsten. ‡ However, it has been shown that due to its operation principle the heating of the cathode is strongly inhomogeneous [37]. Specifically, since a growing fraction of the current flowing through the cathode in the center leaves into the plasma, the current flowing through the central part is higher than that in the outer part. This results in a higher temperature of the inner turns of the spiral, by up to a few hundreds of K. Considering this behaviour, it was further showed that the effect of this temperature inhomogeneity on the total current injection can be modelled via the use of a correction factor to $\overline{T_W}$ [37]. Error bars for the corrected I_{em} are then estimated to be about 15%, accounting primarily for a $\Delta r = \pm1$ μm variation in the cathode radius, and secondarily for a realistic 5% error in the correction factor. Lastly, because it was observed that the cathode temperature increases during a plasma shot, $\overline{T_W}$ was always measured at the end of the plasma shot [37]. The corrected cathode temperature allows to compute the maximum emitted current I_{em} from Richardson law. Here we consider that I_{em} is a correct estimate of the emitted current as long as no virtual cathode is present, which is expected to hold for high enough plasma densities, and when the bias V_b is sufficiently negative with respect to the plasma potential [29, 44, 45]. Note also that the cathode temperature T_W is primarily controlled by Joule heating and thus by the value of the heating current I_h. However

‡ We use the best power-law fit in the range [1800 K; 3200 K] of the thermal expansion corrected resistivity $\rho_W = 5.31\ 10^{-11} T_W^{1.22} - 1.56\ 10^{-9}$ where ρ_W is expressed in Ω/m and T_W in K. It leads to an estimate of the average temperature as $\overline{T_W} = \left[\left(\frac{\pi r_W^2}{l_W}\frac{V_h}{I_h} + 1.56\ 10^{-9}\right)\frac{10^{11}}{5.31}\right]^{\frac{1}{1.22}}$.

the cathode bias V_b has also an influence on T_W due to heating from ion bombardment on the cathode [37]. As a consequence, the emitted depends on the bias V_b, even when the heating current I_h is kept constant.

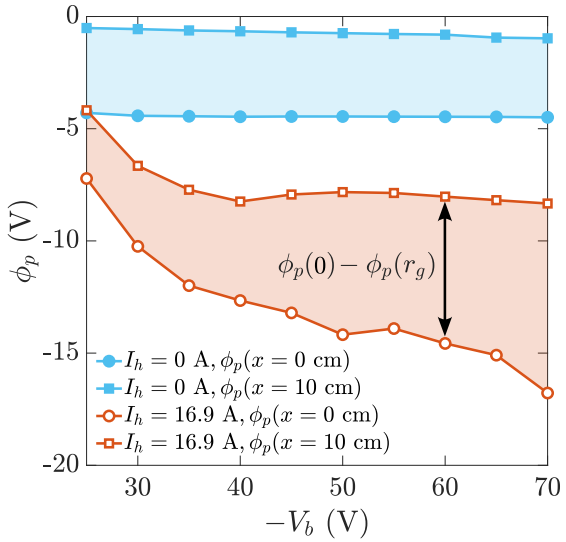

Figure 2: Evolution of the plasma potential in configuration III as a function of the electrode bias $-V_b$ for a cold (full blue) and an emissive (open red) cathode at the center of the plasma column (circles) and in front of the anode located at $x = 10$ cm (squares).

3. Plasma potential control via current injection

3.1. Effective drive of the plasma potential at high current injection

The evolution of the plasma potential ϕ_p as a function of the electrode bias $-V_b$, for both a cold and a hot thermionic cathode at a constant heating current I_h, is shown in figure 2 for configuration III (1 mTorr, 340 G). Note that the abscissa represents $-V_b$ so that the biasing gets stronger from left to right. Both the plasma potential at the center of the plasma column, $\phi_p(x = 0)$ (circles), and at the outer edge, $\phi_p(x = r_g = 10$ cm) (squares), are displayed.

For the cold electrode case (full blue symbols), the plasma potential is observed to be independent of the voltage bias V_b. It is also found that the plasma potential at the outer edge of the plasma column is close to zero ($\Phi_p(x = 10cm) \sim -0.5$V in Fig. 2), as expected given the proximity to the large grounded anode. We stress here the existence of a lateral recess at the probe location (see Fig. 1a), that explains the existence of this finite value. We also note that the measurement of the plasma potential using emissive probes has an accuracy of the order of 0.5 V [39, 45]. In

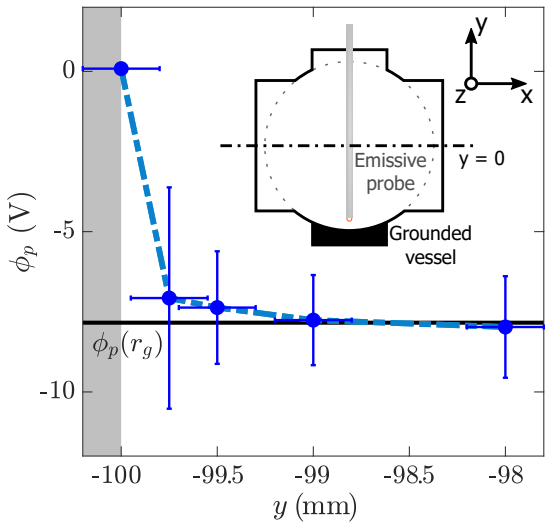

Figure 3: ϕ_p in the anode sheath in configuration III, $V_b = -45$ V and $I_b = 4.2$ A. The grounded wall is represented by the gray area for $y \leq -100$ mm. The black solid line represents the average plasma potential at the anode $\phi_p(r_g)$.

contrast, when the electrode is hot (open red symbols), it is found that the plasma potential responds to a change in electrode bias. Looking more closely, both $\phi_p(x = 0)$ and $\phi_p(x = r_g)$ are affected by an increase of $-V_b$. Consequently, the plasma potential of the entire plasma column is significantly lowered: a large anode sheath of a few T_e, with $T_e \simeq 2$ eV at the sheath entrance in configuration III, is observed at the outer edge of the column, and the radial potential drop across the plasma column increases with $-V_b$.

Let us first comment on the main features of the anode sheath. Its spatial structure was probed in configuration III by inserting an emissive probe along the vertical axis y, with a home-made aluminum flange filling the DN 100 access port at $y = -r_g$. The obtained evolution of the plasma potential as a function of position in the sheath is shown in figure 3, with errorbars representing the standard deviation of the plasma potential fluctuations. This scan shows conclusively the existence of an electron sheath at the anode, whose thickness is less than a few hundreds of microns. Yet, the in-depth study of a thin sheath structure requires dedicated setup and thinner emissive probes, and no robust experimental measurement of the anode sheath scalings was successfully conducted in this study. Possible scalings with the Debye length or the electron Larmor radius thus remain unclear, and the underlying mechanisms responsible for this structure are still under investigation [46]. Given these uncertainties, we will not consider in the remainder of this study the effect of the sheath, and will simply

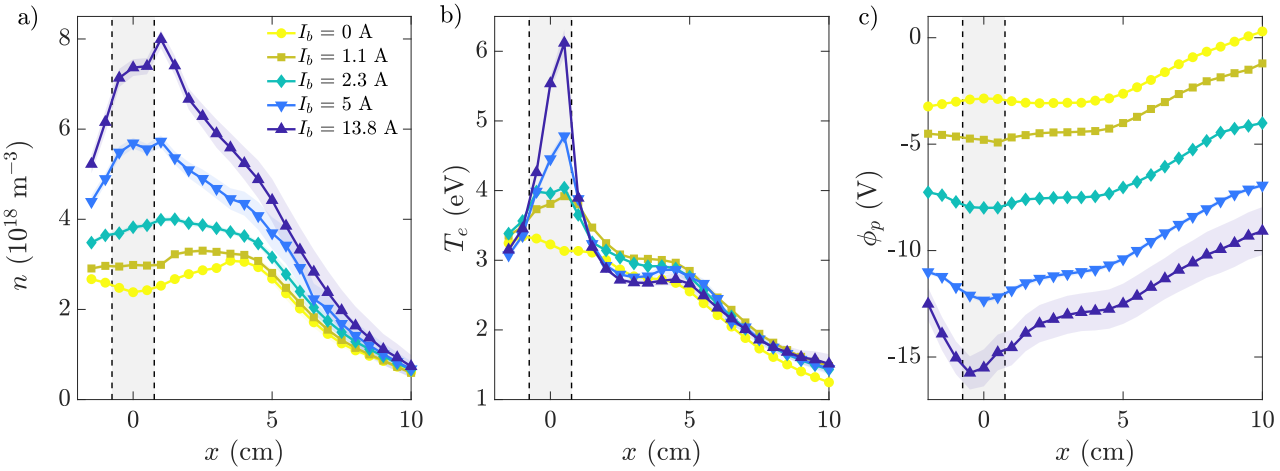

Figure 4: *a)* Plasma density, *b)* electron temperature and *c)* plasma potential profiles in configuration II for V_b = -60 V for several injected current I_b. I_b is controlled by the heating current I_h. The gray area represents the position of the cathode.

write $\phi_p(x = r_g)$ the plasma potential at the entrance to the anode sheath, *i.e.* the value defined in the range $-99.5 < y \leq -98$ mm in figure 3.

Another motivation to disregard here the contribution of the sheath and consider instead only the evolution with the electron current injection of the radial potential drop across the plasma column $\phi_p(0) - \phi_p(r_g)$, as shown in figure 2, is that it can be directly compared with the models described in section 4. This will be the object of section 5. Prior to discussing models, we however first characterize the response to thermionic current injection by analyzing spatially-resolved profiles of plasma parameters obtained at fixed cathode bias but variable thermionic current, controlled by a modification of the heating current I_h. Indeed, while the evolution of the plasma potential with the cathode bias V_b and constant heating current I_h shown in figure 2 is highly illustrative, this was not achieved at constant thermionic emission I_{em} since the cathode temperature depends on V_b, as discussed further in section 5.

3.2. Spatially resolved plasma parameters

The evolution of the radial profile (measured along the x-axis) of the plasma parameters with increasing current injection and constant bias is shown in figure 4 for P_w = 1 kW in configuration II (2 mTorr, 240 G) and V_b = -60 V. Current injection is controlled by the cathode temperature (see equation 2), through the value of I_h. The gray area corresponds to the location of the cathode. The slight asymmetry with respect to $x = 0$ cm is believed to result from the shadowing introduced by the probe shaft. Complementary radial scans of the plasma parameters for configurations I and III, at $V_b = -60$ V, can be found in figures C1 and C2 in Supp. Mat. C. The standard deviations of the fluctuations are shown in these graphs by the light-colored area around the time-averaged data. Note that the $I_b = 0$ case corresponds to a floating cold cathode, whose plasma properties closely resemble those of the biased cold cathode case, which is not included here for clarity.

Let us first investigate the influence of current injection on the plasma density and the electron temperature. Large current injection significantly increases plasma density, more specifically in the central region $x \leq 5$ cm. This increase is believed to result from primary emitted electrons, with an energy $|\phi_p - V_b|$ larger than the ionization energy for argon $\epsilon^* = 15.8$ eV. Furthermore, a sharp increase of the electron temperature T_e is observed for $|x| \leq 1$ cm. As discussed in Supp. Mat. A, this increase in T_e is likely due to the quick thermalization of the energetic primary electrons. This localized electron temperature bump restricted to $x \leq 1$ cm, is an evidence for the strong magnetization of electrons. The increase in electron temperature at the center enhances ionization in the core, compared with the $I_b = 0$ A case, as observed in figure 4a).

Let us now detail the evolution of the plasma potential radial profile at fixed cathode bias V_b. Current injection is observed to have a strong influence at the edge of the plasma column, thus confirming the formation of a large anode sheath up to a few T_e (*i.e.* $\approx$ 10 V with $T_e \simeq 1.5$ eV in configuration II), as discussed above. Closer examination also shows an increase of the radial potential drop across the plasma column with I_b. In particular, the sign of $\partial\phi_p/\partial r$ at $|x| \leq 2$ cm reverses when current injection increases, leading to a reversal of the plasma rotation [32].

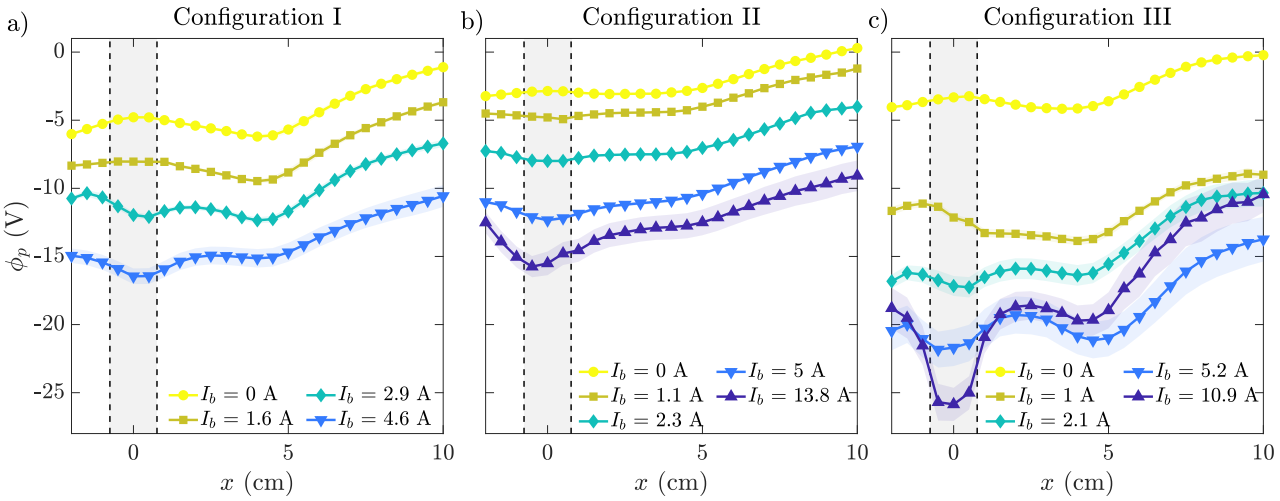

Figure 5: Plasma potential profiles versus x for configurations I (a), II (b) and III (c) at $V_b = -60$ V. The gray area represents the position of the cathode.

Complementary measurements of radial profiles of the plasma potential at $V_b = -40$ V and for increasing values of the current injection are shown in figure D1 in Supp. Mat. D. For comparable values of the injected current I_b, similar radial profiles were measured when the cathode is biased at $V_b = -40$ and -60 V. This observation suggests that, in these regimes, the radial potential drop is mainly controlled by current injection, and is independent of cathode bias, in agreement with operation in a *saturated* regime, as detailed in the model recalled in section 4 [1].

Note finally that the modification of the plasma parameters may jeopardize the global plasma stability. For instance, the important standard deviation of ϕ_p at $I_b = 13.8$ A indicates the growth of significant ϕ_p coherent fluctuations, in the kHz range, that are not further detailed. The work presented herein focuses on quiescent regimes.

3.3. Influence of neutral pressure and magnetic field on the plasma potential

As further detailed in section 4, the potential drop in the plasma column is controlled by the plasma electrical conductivity perpendicular to the magnetic field, which depends on the neutral density n_n and magnetic field intensity B for given values of the plasma parameters The influence of neutral density and magnetic field on the plasma potential profiles is shown in figure 5 for the three configurations at cathode bias $V_b = -60$ V. Each configuration is displayed in a different panel (configurations I to III from left to right), and the colors code for increasing values of I_b. A similar dataset for $V_b = -40$ V is available in figure E1 in Supp. Mat. E.

The existence of the anode sheath and the increase of the plasma potential drop across the plasma column as current injection increases are observed for all three configurations. A marked dependence of the plasma potential profiles on the experimental parameters B and p_0 is noted, whereas comparison with figure C1 shows a weaker dependence on V_b. We note here that B^2/n_n is identical in configuration I and II, but increases by a factor 4 when moving from configuration I and II to configuration III.

4. Modeling the radial potential drop

The goal of this section is to present briefly the analytical model of plasma potential control using an emissive cathode and described thoroughly in [1]. In section 5, it will then be confronted quantitatively to the experimental dataset detailed above.

4.1. Model description

The biased cathode is modelled as a disk of radius r_b, biased at a homogeneous potential V_b. The external cylindrical vessel of radius r_g and length L is grounded, while the end caps are insulating for $r_b < r < r_g$. Hence the current at the cathode I_b, mainly constituted of the ion saturation current from the plasma I_{is} and the thermionic current from the cathode I_{em}, flows from the anode, *i.e.* the wall, to the cathode as shown in schematically in the left panel of figure 6.

The model computes the plasma potential spatial distribution by solving the local Ohm's law, given the anisotropic electrical conductivities and the imposed electron and ion fluxes at the cathodes [24]. For the conditions of interest here the perpendicular electrical

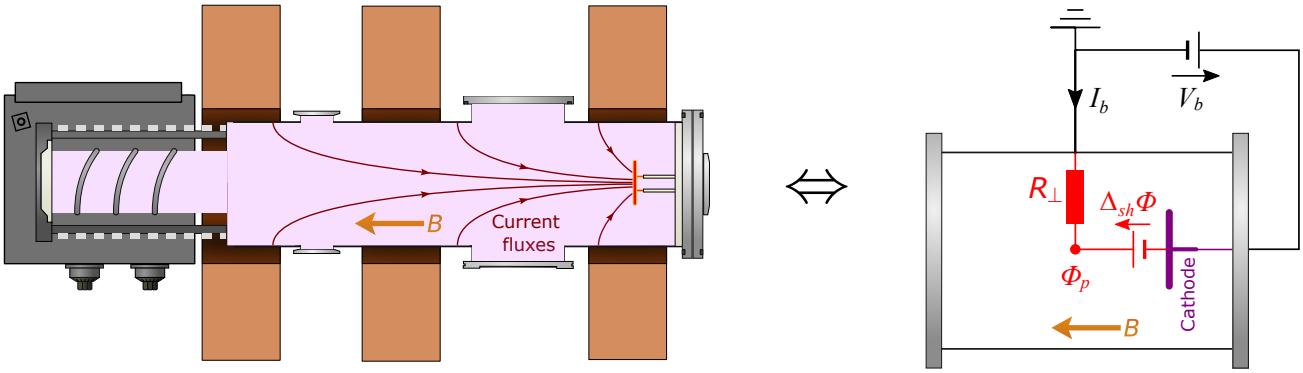

Figure 6: *Left:* Current fluxes in the plasma device, from the anode (grounded walls) to the emissive cathode. *Right:* Simplified equivalent electrical circuit. The plasma exhibits a large resistance perpendicular to the magnetic field $R_\perp$. The current I_b induces a potential drop from the lateral wall to the plasma core via Ohm's law, and affects plasma potential ϕ_p. The sheath potential drop at the cathode $\Delta_{sh}\phi$ self-adjusts to match ϕ_p with the cathode bias V_b.

conductivity $\sigma_\perp$ is driven by ion-neutral collisions and is expressed as the Pedersen conductivity, while the parallel conductivity $\sigma_\parallel$ is dominated by the contribution of electrons. In this limit the conductivities can be approximated by [24]:

$$\sigma_\parallel = \frac{ne^2}{m_e\left(\nu_{en}+\nu_{ei}\right)} \tag{5}$$

$$\sigma_\perp = \frac{ne^2}{m_i\nu_{in}\left(1+\omega_{c,i}^2/\nu_{in}^2\right)} \tag{6}$$

with $\nu_{\alpha\beta}$ the collision rate between species α and β (see Supp. Mat. G for expressions of these rates). When ions are magnetized (*i.e.* $\omega_{c,i}^2/\nu_{in}^2 \gg 1$), the perpendicular conductivity reads:

$$\sigma_\perp^m = \frac{nm_i\nu_{in}}{B^2} \tag{7}$$

Since the ion-neutral collision frequency ν_{in} is proportional to the neutral density n_n, $\sigma_\perp^m$ scales as B^2/n_n. Given the values of the ratio $\omega_{c,i}/\nu_{in}$ shown in table 1, $\sigma_\perp^m$ is a relevant approximation for $\sigma_\perp$ at leading order, especially for configurations I and III. Note here that while equations (5) and (6) are good approximations in this experiment and are useful to derive parametric dependencies, we use comprehensive expressions accounting both for Coulomb and neutral collisions $\sigma_{\perp,\mathrm{all}}$ and $\sigma_{\parallel,\mathrm{all}}$ [47, 48] in solving Ohm's law. Also, while reference [24] considered the possibility for a potential drop along magnetic field lines, it is neglected here in light of the low value $\sigma_\perp/\sigma_\parallel = 10^{-3} \ll 1$. The plasma potential is thus considered homogeneous along the magnetic field. Under these simplifying hypotheses the current driven from the anode to the cathode results only in a radial potential drop $\Delta_\perp\phi$ and a cathode sheath potential $\Delta_{sh}\phi$. By construction the latter varies and matches the difference between the cathode bias V_b and the radial potential drop $\Delta_\perp\phi$. The equivalent electrical circuit is represented in the right panel of figure 6.

From this model, the potential drop across the plasma column is $\Delta_\perp\phi = \phi_p(r_b) - \phi_p(r_g) = -R_\perp^{(model)} I_b$ with

$$R_\perp^{(model)} = \int_{r_b}^{r_g} \frac{\mathrm{d}r}{\sigma_{\perp,\mathrm{all}}(r)2\pi Lr}. \tag{8}$$

the perpendicular resistance between the outer radius of the electrode r_b and the external wall r_g. In cases where the electrode only collects ions from the plasma (*i.e.* a negatively biased cold cathode), an important result of this simple model is that the most negative potential drop is $R_\perp^{(model)} I_{is}$, or, normalizing this voltage by the electron temperature T_e, $\chi^{-1} = R_\perp^{(model)} I_{is}/T_e$.

This simple model also exposes immediately the added control brought in by current injection. Indeed, for a negatively biased emissive cathode $I_b \sim I_{is} + I_{em}$ (the electron contribution is neglected for sufficiently negative biases), which means that the current flowing through the resistance is $(1+\Xi)$ larger, with $\Xi = I_{em}/I_{is}$ defined as the ratio of thermionic to ion saturation current. The most negative potential drop is $R_\perp^{(model)}(1+\Xi)I_{is}$, or, in dimensionless units, $(1+\Xi)\chi^{-1}$. It is therefore $(1+\Xi)$ times the cold electrode limit. One can also emphasize that Eq. 8 does not depend on the heterogeneous spatial distribution of thermionic emission, but only on the total current at the cathode I_b. Plasma potential in the cathode shadow is not investigated here and would require further investigation.

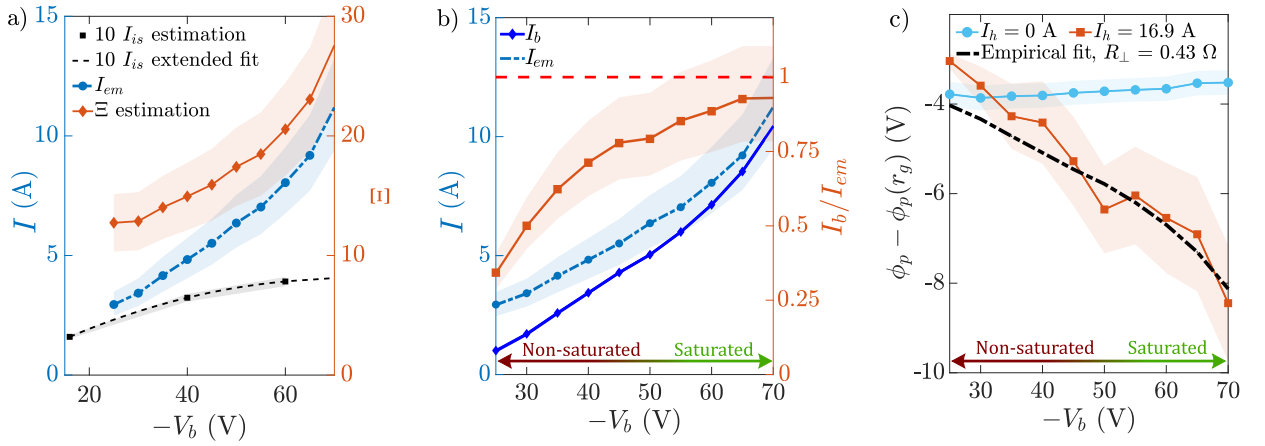

Figure 7: Currents and potential drop as a function of the electrode bias $-V_b$ for the data presented in figure 2 (hot case), measured in configuration III. The cathode is at constant heating. *a)* Left scale: I_{em} (blue circles) and I_{is} (black squares, magnified 10 times for better readability) estimations. Right scale: estimation of the Ξ number (orange diamonds). *b)* Left scale: Total current at the cathode I_b and emitted current I_{em} (blue symbols). Right scale: I_b/I_{em} ratio (orange symbols). *c)* Radial potential drop $\phi_p(0) - \phi_p(r_g)$ for the cold and hot cathode. The dashed line corresponds to an empirical best fit $R_\perp I_b$.

4.2. Predicted regimes of operation and parametric dependencies

Putting these pieces together, two regimes of operation of a hot cathode can be identified, as a function of the dimensionless parameters χ and Ξ.

Non-saturated regime. This regime is characterized by a non-zero electron current I_e drawn from the plasma by the cathode. It is expected for weak cathode biases, $|V_b/T_e| \leq (1+\Xi)\chi^{-1}$. In this regime, the plasma potential ϕ_p largely follows the bias applied to the cathode, other than for the classic floating sheath offset ΛT_e with Λ the sheath parameter introduced in section 2. The plasma potential accordingly reads $\phi_p = V_b + \Lambda T_e$.

Saturated regime. This regime is observed at stronger cathode bias, $|V_b/T_e| > (1+\Xi)\chi^{-1}$. In this regime the electron current drawn from the plasma vanishes, *i.e.* $I_e = 0$. As a result I_b does not vary with applied bias since both I_{is} and I_{em} do not depend on V_b. The potential drop across the plasma column $\Delta_\perp\phi$ is then constant and equal to $-R_\perp^{(model)} I_b$ for any cathode bias V_b, leading to a most negative plasma potential in front of the cathode

$$\phi_p^{sat} = -R_\perp^{(model)} I_b = -(1+\Xi) R_\perp^{(model)} I_{is} \tag{9}$$

The plasma potential in the saturated regime can hence be controlled via current injection and the parameter Ξ. The difference between the applied bias V_b and the saturated value of the plasma potential ϕ_p^{sat} is the potential drop across the sheath $\Delta_{sh}\phi$, which increases as V_b is lowered for fixed Ξ factor. For a homogeneous plasma column, at strong thermionic emission $\Xi \gg 1$ and when considering the magnetized perpendicular conductivity $\sigma_\perp^m$ (equation (7)), the saturated value of the plasma potential scales as

$$\phi_p^{sat} \propto \frac{-1}{\sqrt{T_i m_i}} \frac{B^2}{n_n} \frac{I_{em}}{n} \tag{10}$$

Note that control through Ξ as suggested by the model assumes a monotonic ion sheath, and would in particular need to be reconsidered in the presence of a virtual cathode. Yet, for the plasma parameters typically used in VKP, a virtual cathode regime is not expected for $\Xi \lesssim 100$. Since the experiment operates well below this limit, this issue can be safely excluded here. A curious reader may however refer to specialized works on that particular matter (see references [29, 44]).

4.3. Basic differences between model and experiment

Having presented the main properties and results of the model, we now underline a number of basic differences between model hypotheses and experiment, which should be kept in mind when interpreting experimental data in light of model predictions in section 5.

First, and maybe most importantly, the model assumes a ground condition at the outer edge of the plasma column $\phi_p(r_g) = 0$, and thus does not account for an anode sheath. To circumvent this issue we will restrict the comparison between experimental data and predictions to the radial potential drop within the plasma column, excluding the anode sheath. Second, the model considers an ideal homogeneous cathode

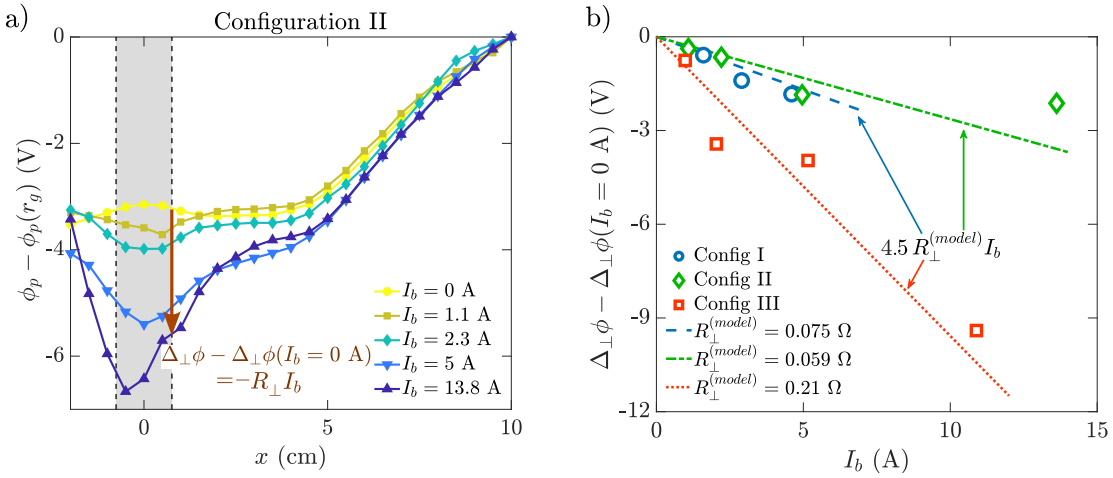

Figure 8: *a)* Radial plasma potential profile, offset to 0 V at $x = 10$ cm, in configuration II, $V_b = -60$ V. The gray area indicates the position of the cathode. *b)* Radial potential drop at the plasma core as a function of I_b: experimental results (markers), and $4.5R_\perp^{(model)} I_b$ (dashed lines).

while the spiral cathode exhibits inhomogeneities in temperature and voltage [37]. Third, the model assumes a uniform zero plasma potential in the absence of current injection, while experiments reveal a non-zero radial plasma potential profile (see the case $I_b = 0$ A in figure 4a)). This feature will be further discussed in section 5.

5. Potential drop across the plasma column: comparison between the experimental data and the model

5.1. Transition from a non-saturated to a saturated regime

A first question one can ask is how the model described above can shed light onto the differences in the response to biasing for cold and hot electrode observed in figure 2. In the cold cathode case, the cathode bias V_b does not affect the value of the plasma potential since the cathode current reaches the ion saturated current $I_{is} \simeq 0.2$ A and weakly evolves with V_b (See Supp. Mat. E showing the evolution of I_b with V_b). This observation confirms the low-efficiency of cold cathodes ($\Xi = 0$) for plasma potential control.

Regarding the hot cathode case, we first plot in figure 7a) the currents I_{em} and I_{is} as a function of $-V_b$ for the conditions reported in figure 2, *i.e.* in configuration III for a constant heating current I_h. The Richardson current I_{em} was computed according to the method presented in section 2, for each value of V_b. As shown in previous work [37], the strong dependency of I_{em} on V_b does not come from Schottky nor space-charge limited effects, but from an enhanced ion bombardment and a strong cathode self-heating due to its filamentary structure. The ion saturation current I_{is} at the cathode (black squares, left scale) was computed from measurement of the ion saturation current of a small Langmuir probe at $-V_b = \{16; 40; 60\}$ V with a 5% uncertainty highlighted by the gray area, and extrapolated using an empirical second-order polynomial fit. An estimate of $\Xi = I_{em}/I_{is}$ is then obtained (orange diamonds, right scale), with 20% errorbars. The first observation here is that Ξ is not constant, though the heating current I_h is kept constant, and increases from 10 to 30 as $-V_b$ increases. This is in contrast with the model where V_b and Ξ are considered independent. Consequently, it is difficult to disentangle the influences of Ξ and V_b on the evolution of the plasma potential observed in figure 2.

The regime of operation is then evaluated from the value of the ratio I_b/I_{em}. Figure 7b) shows the evolution of the measured cathode current I_b (dark blue) and the computed Richardson current I_{em} (light blue) as a function of $-V_b$, as well as the value of I_b/I_{em} (orange squares, right-hand axis), which is a reasonable proxy of the nature of the regime. Specifically, $I_b/I_{em} < 1$ corresponds to a non-saturated regime, since a non-negligible electron current is drawn from the plasma. Conversely $I_b/I_{em} \sim 1$ corresponds to a saturated regime. A transition from a non-saturated to a saturated regime is thus observed for increasing values of $-V_b$, with a smooth transition at $-V_b \sim 50$ V. Since $-V_b$ affects the cathode temperature [37], Ξ is not kept constant for the bias voltage scan reported in figure 7. As a result, the potential drop increases with the absolute value of the voltage bias in the saturated regime, in stark contrast to the model predictions where Ξ is independent of V_b.

The evolution of the voltage across the plasma

column $\phi_p(0) - \phi_p(r_g)$ with $-V_b$ is shown in figure 7c) for the cold and hot electrode cases. Errorbars represent the standard deviation of the plasma potential temporal fluctuations. As already noted $\phi_p(0) - \phi_p(r_g)$ remains constant in the cold cathode case, whereas it increases with $-V_b$ in the emissive case: current injection from a hot cathode thus improves control over the plasma potential profile. Furthermore, the smooth transition from a non-saturated to a saturated regime in the hot cathode case for $-V_b \sim 50$ V is confirmed by a change in the response of the potential drop $\phi_p(0) - \phi_p(r_g)$ to the applied bias $-V_b$. In the saturated regime, the potential drop is well fitted as a product $R_\perp I_b$. Using the measured values of I_b, the best linear fit for $-V_b > 50$ V gives $R_\perp = 0.43\ \Omega$ (black dashed line in figure 7c)), in agreement with model predictions $R_\perp^{(model)} \in [0.1, 1]\ \Omega$ for the parameters under investigation.

5.2. Scaling laws in the saturated regimes

Let us now examine here how the response of the potential radial drop $\Delta_\perp\phi = \phi_p(r_b) - \phi_p(r_g)$ to current injection varies with operating conditions, and in particular with the magnetic field and neutral pressure (configurations I to III in table 1). The spatially-resolved plasma potential profiles displayed in figure 4c) for configuration II, are shown in figure 8a) when shifted to 0 V at the outer edge, *i.e.* $\phi_p - \phi_p(r_g)$. This allows to highlight the radial potential drop across the plasma column, regardless of the potential drop at the anode sheath.

As already noted in section 4.3, the model assumes a uniform zero plasma potential in the absence of current injection, while experiments reveal a non-uniform radial plasma potential profile when $I_b = 0$ A. Since the radial potential profile when $I_b = 0$ is not captured in the model, we choose to subtract it from the plasma potential profile at finite I_b, *i.e.* we consider $\Delta_\perp\phi(I_b) - \Delta_\perp\phi(I_b = 0)$. This quantity is highlighted by a brown downward arrow in figure 8a), and will now be compared with model predictions. This procedure implicity assumes that the measured radial potential drop $\Delta_\perp\phi(I_b)$ is the sum of two components: the potential drop with no current injection $\Delta_\perp\phi(I_b = 0)$, and an additional potential drop due to current injection. This is a strong assumption that is likely to fail at large I_b, for which the plasma density and electron temperature profiles are significantly modified (see figure 4), and new instabilities may arise.

The evolution of $\Delta_\perp\phi(I_b) - \Delta_\perp\phi(I_b = 0)$ with respect to I_b at $V_b = -60$ V for the three configurations is displayed in figure 8b). Note that the normalized thermionic emission values Ξ are given in table E1 in Supp. Mat. H for every spatially-resolved scan at $V_b = -60$ V. A linear trend with I_b is observed

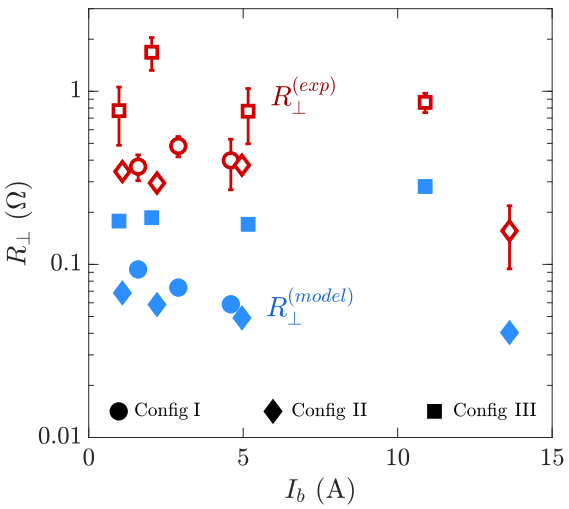

Figure 9: Perpendicular resistance values at $V_b = -60$ V for the three configurations: model values from equation (8) (full blue markers) and experimental values from equation (11) (open red symbols).

for all configurations, which is consistent with a fully saturated regime. This further supports the interpretation of a potential drop driven by current injection $\Delta_\perp\phi(I_b) - \Delta_\perp\phi(I_b = 0) = -R_\perp I_b$. An important observation is that $R_\perp$, is similar for configurations I and II, and nearly 4 times larger for configuration III. This is in remarkable agreement with the scaling law B^2/n_n predicted by the model (see equation (10)).

While experimental data shows remarkable agreement with the behaviour and parametric trends predicted by the model, a quantitative comparison of the perpendicular resistance $R_\perp$ reveals systematic deviations. This is shown in figure 8b), where $R_\perp$ estimated from equation (8) using the spatially-resolved plasma parameters measured in each case are about 4.5 smaller that those estimated from experimental data. Specifically, using an ion temperature $T_i = 0.2$, 0.28 and 0.45 eV, the perpendicular resistance $R_\perp^{(model)}$ is computed to be 0.075, 0.059 and 0.21 Ω (respectively for configuration I, II and III). Note that the ion temperatures used here were measured at 1 mTorr [40], and should be taken with caution for configuration II.

Figure 9 displays the evolution of the experimentally measured perpendicular resistance, defined as

$$R_\perp^{(exp)} = \frac{\Delta_\perp\phi(I_b) - \Delta_\perp\phi(I_b = 0)}{I_b}, \tag{11}$$

together with the value obtained from the model $R_\perp^{(model)}$ for all three configurations and $V_b = -60$ V. Error bars for $R_\perp^{(exp)}$ are computed from the standard deviation of the plasma potential measurements.

The first observation is that, for a given configuration, the values of the perpendicular resistance $R_\perp$ stay approximately constant as the injected current I_b increases. This suggests that the parameters of the plasma column weakly evolve with I_b, in the range of current injection investigated here. This observation justifies a-posteriori the strong assumption made in subtracting the radial potential drop at zero emission and to consider $\Delta_\perp\phi(I_b) - \Delta_\perp\phi(I_b = 0)$. The second observation is that the systematic discrepancy observed between the measured values $R_\perp^{(exp)}$ and the model values $R_\perp^{(model)}$ is also independent of the value of I_b, showing the robustness of the B^2/n_n scaling at leading order.

Let us now briefly mention possible explanations for this quantitative discrepancy, focusing particularly on magnetized cases (configurations I and III). The computation of the perpendicular resistance requires a precise estimate of the neutral density n_n as $R_\perp^{(model)} \propto n_n^{-1}$. In the regime of operation reported here, significant neutral depletion or neutral heating may occur [49, 50], which could lead to an underestimation of the perpendicular resistance by up to a factor 5. A second source of discrepancy may lie in the evaluation of the ion temperature T_i; in particular for configuration II for which T_i was extrapolated.

6. Conclusion

This work has explored the effect of current injection from an emissive cathode on the evolution of the radial plasma potential profile in a magnetized plasma column, for various magnetic field and neutral filling pressure. We have reported an efficient plasma potential control using a strongly emissive cathode as compared to a cold electrode. The ratio of emitted current with the ion saturation current $\Xi = I_{em}/I_i$ appears to be the relevant control parameter for the plasma potential control, independently of dimensionless cathode bias V_b/T_e, at large biases. The experimental observations are in very good qualitative agreement with the model developed by Trotabas and Gueroult [1]: the radial potential drop is controlled by the value of the perpendicular resistance $R_\perp$ of the plasma column, and thus evolves as $R_\perp I_b$. In particular, the potential drop across the plasma column satisfies a B^2/n_n scaling, at leading order.

The model underestimates the perpendicular resistance by a factor four to five. A better qualitative comparison would require spatially-resolved neutral density and precise ion temperature measurements. The influence of finite axial resistivity on the efficiency of the plasma potential control was investigated theoretically in Ref. [1], but the present experimental configuration was not adapted to study its influence in details. Axially resolved scans of the plasma parameters would provide valuable informations to confirm the predictions. The distance between current injection and the plasma source is also an important parameter that could not be investigated in our configuration. We expect that when the thermalization of the emitted electrons is smaller than the length of the plasma column, and when $\sigma_\perp/\sigma_\parallel \ll 1$, no strong axial dependence should be observed. Strong axial gradients may arise when the thermalization length would be similar to the length of the plasma column. The dataset shown in this article strongly supports a B^2/n_n scaling for the plasma potential drop; the validity of this scaling could usefully be checked from an extended dataset obtained in other plasma devices. Besides, we reported the existence of a large electron sheath at the anode, which is currently not included in models. Dedicated experiments focusing on the properties of this anode sheath would help building a fully consistent model in the presence of current injection. Additionally, strong electron injection was found to destabilize the plasma column and gives rise to intense coherent fluctuations, that should be taken into account to compute possible contribution of turbulent fluctuations in the plasma resistivity.

Acknowledgements

The authors acknowledge fruitful discussions with Cécile Arnas, Ivo Furno, Stéphane Heuraux and Sedina Tsikata.

Author Declarations

Conflict of Interest

The authors have no conflicts to disclose.

Data availaility

The data that support the findings of this study are available from the corresponding author upon reasonable request.

Author Contributions

Francis Pagaud: Conceptualization (supporting); Data curation (lead); Formal analysis (lead); Investigation (equal); Resources (supporting); Software (equal); Writing - original draft (lead); Writing - editing (equal).
Vincent Dolique: Conceptualization (supporting); Investigation (supporting); Resources (supporting); Writing - editing (supporting).
Simon P. H. Vincent: Conceptualization (supporting);

Formal analysis (supporting); Investigation (supporting); Resources (supporting); Writing - editing (supporting).
Baptiste Trotabas: Conceptualization (supporting); Formal analysis (supporting); Investigation (supporting); Resources (supporting); Software (equal).
Renaud Gueroult: Conceptualization (equal); Formal analysis (supporting); Funding acquisition (supporting); Investigation (equal); Resources (supporting); Software (supporting); Writing - original draft (support); Writing - editing (equal); Supervision (supporting).
Nicolas Plihon: Conceptualization (equal); Data curation (supporting); Formal analysis (supporting); Funding acquisition (lead); Investigation (equal); Resources (lead); Software (supporting); Writing - original draft (supporting); Writing - editing (equal); Supervision (lead).

References

[1] Trotabas B and Gueroult R 2022 *Plasma Sources Sci. Technol.* **31** 025001

[2] Wagner F, Becker G, Behringer K, Campbell D, Eberhagen A, Engelhardt W, Fussmann G, Gehre O, Gernhardt J, Gierke G v, Haas G, Huang M, Karger F, Keilhacker M, Klüber O, Kornherr M, Lackner K, Lisitano G, Lister G G, Mayer H M, Meisel D, Müller E R, Murmann H, Niedermeyer H, Poschenrieder W, Rapp H, Röhr H, Schneider F, Siller G, Speth E, Stäbler A, Steuer K H, Venus G, Vollmer O and Yü Z 1982 *Physical Review Letters* **49** 1408–1412 publisher: American Physical Society

[3] Schirmer J, Conway G, Zohm H, Suttrop W and Team t A U 2006 *Nuclear Fusion* **46** S780

[4] Burrell K H 1997 *Phys. Plasmas* **4** 1499–1518

[5] Oost G V, Adámek J, Antoni V, Balan P, Boedo J A, Devynck P, Ďuran I, Eliseev L, Gunn J P, Hron M, Ionita C, Jachmich S, Kirnev G S, Martines E, Melnikov A, Schrittwieser R, Silva C, Stöckel J, Tendler M, Varandas C, Schoor M V, Vershkov V and Weynants R R 2003 *Plasma Phys. Control. Fusion* **45** 621

[6] Lehnert B 1973 *Phys. Scr.* **7** 102

[7] Zweben S J, Gueroult R and Fisch N J 2018 *Phys. Plasmas* **25** 090901

[8] Gueroult R, Rax J M and Fisch N J 2018 *J. Cleaner Prod.* **182** 1060–1069

[9] Liziakin G, Antonov N, Usmanov R, Melnikov A, Timirkhanov R, Vorona N, Smirnov V S, Oiler A, Kislenko S, Gavrikov A and Smirnov V P 2021 *Plasma Phys. Control. Fusion* **63** 032002 publisher: IOP Publishing

[10] Tsushima A and Sato N 1991 *J. Phys. Soc. Jpn.* **60** 2665–2672 publisher: The Physical Society of Japan

[11] Desjardins T R and Gilmore M 2016 *Phys. Plasmas* **23** 055710

[12] Desjardins T R and Gilmore M 2018 *Phys. Plasmas* **25** 062117

[13] Yoshinuma M, Inutake M, Hatakeyama R, Kaneko T, Hattori K, Ando A and Sato N 1999 *Phys. Lett. A* **255** 301–306

[14] DuBois A M, Eadon A C and Thomas Jr E 2012 *Phys. Plasmas* **19** 072102

[15] Thomas Jr E, Jackson J D, Wallace E A and Ganguli G 2003 *Phys. Plasmas* **10** 1191–1194

[16] Thomas Jr E, Eadon A and Wallace E A 2005 *Phys. Plasmas* **12** 042109

[17] Sakai O, Yasaka Y and Itatani R 1993 *Phys. Rev. Lett.* **70** 4071

[18] Shinohara S and Matsuyama S 2002 *Phys. Plasmas* **9** 4540–4550

[19] Vincent S, Dolique V and Plihon N 2022 *Phys. Plasmas* **29** 032104

[20] Aggarwal S, Camenen Y, Escarguel A and Poyé A 2023 *J. Plasma Phys.* **89** 905890310

[21] Thakur S C, Brandt C, Cui L, Gosselin J J, Light A D and Tynan G R 2014 *Plasma Sources Sci. Technol.* **23** 044006

[22] Taylor R J, Brown M L, Fried B D, Grote H, Liberati J R, Morales G J, Pribyl P, Darrow D and Ono M 1989 *Phys. Rev. Lett.* **63** 2365–2368

[23] Gueroult R, Tripathi S K P, Gaboriau F, Look T R and Fisch N J 2024 *J. Plasma Phys.* **90** 905900603

[24] Gueroult R, Rax J M and Fisch N J 2019 *Phys. Plasmas* **26** 122106

[25] Baalrud S D, Scheiner B, Yee B T, Hopkins M M and Barnat E 2020 *Plasma Sources Sci. Technol.* **29** 053001

[26] Liziakin G, Gavrikov A and Smirnov V 2020 *Plasma Sources Sci. Technol.* **29** 015008

[27] Liziakin G, Oiler A, Gavrikov A, Antonov N and Smirnov V 2021 *J. Plasma Phys.* **87** 905870414

[28] Trotabas B 2022 Ph.d. thesis Université de Toulouse 3

[29] Poulos M J 2019 *Phys. Plasmas* **26** 022104

[30] Van Compernolle B, Poulos M J and Morales G J 2019 *Phys. Plasmas* **26** 122102

[31] Jin S, Poulos M J, Van Compernolle B and Morales G J 2019 *Phys. Plasmas* **26** 022105

[32] Désangles V, Bousselin G, Poyé A and Plihon N 2021 *J. Plasma Phys.* **87** 905870308

[33] DuBois A M, Thomas Edward J, Amatucci W E and Ganguli G 2014 *Phys. Plasmas* **21** 062117

[34] Vincent S P H 2021 Ph.d. thesis Université de Lyon

[35] Karbashewski S, Sydora R D, Van Compernolle B, Simala-Grant T and Poulos M J 2022 *Phys. Plasmas* **29** 112309

[36] Plihon N, Bousselin G, Palermo F, Morales J, Bos W J T, Godeferd F, Bourgoin M, Pinton J F, Moulin M and Aanesland A 2015 *J. Plasma Phys.* **81** 345810102

[37] Pagaud F, Dolique V, Claire N and Plihon N 2023 *Plasma Sources Sci. Technol.* **32** 115019

[38] Diebold D, Hershkowitz N, Pew J, Sorensen J, Tanaka T, Tsui H, Ritz C and Wootton A 1992 *J. Nucl. Mater.* **196-198** 789–793

[39] Sheehan J P and Hershkowitz N 2011 *Plasma Sources Sci. Technol.* **20** 063001

[40] Désangles V 2018 Ph.d. thesis Université de Lyon

[41] Konuma M 1992 *Film Deposition by Plasma Techniques* (Berlin, Heidelberg: Springer Berlin Heidelberg)

[42] Tolias P 2014 *Plasma Phys. Control. Fusion* **56** 123002

[43] Herring C and Nichols M H 1949 *Rev. Mod. Phys.* **21** 185–270

[44] Ye M Y and Takamura S 2000 *Phys. Plasmas* **7** 3457–3463

[45] Cavalier J, Lemoine N, Bousselin G, Plihon N and Ledig J 2017 *Phys. Plasmas* **24** 013506

[46] Pagaud F 2024 Ph.d. thesis Université de Lyon

[47] Song P, Gombosi T I and Ridley A J 2001 *J. Geophys. Res. A: Space Phys.* **106** 8149–8156

[48] Rax J M, Kolmes E J, Ochs I E, Fisch N J and Gueroult R 2019 *Phys. Plasmas* **26** 012303

[49] Fruchtman A 2017 *J. Phys. D: Appl. Phys.* **50** 473002

[50] Thakur S C, Simmonds M J, Caneses J F, Chang F, Hollmann E M, Doerner R P, Goulding R, Lumsdaine A, Rapp J and Tynan G R 2021 *Plasma Sources Sci. Technol.* **30** 055014